COMMUNICATION

2D Organic Nanosheets

ADVANCED MATERIALS INTERFACES
www.advmatinterfaces.de

Free-Standing Buckle-Delaminated 2D Organic Nanosheets with Enhanced Mechanical Properties and Multifunctionality

*Qiuting Zhang, Zhuolei Zhang, and Jie Yin**

2D organic conjugated polymer nanofilm has shown promising potential applications in organic solar cells and flexible electronics due to its tunable electronic and mechanical properties. However, its multifunctionality is largely hindered by weak mechanical performances. Here, a new strategy of harnessing buckling-driven delamination is proposed for achieving highly stretchable, free-standing organic nanosheets with largely improved multifunctionality in mechanical, electrical, and wetting properties. A model system of organic conjugated polymeric (P3BT/C60) nanosheets on prestrained elastomers is fabricated through both spin-coating and transfer-printing methods. It is found that the free-standing nanosheet exhibits both superior mechanical and electrical properties with two times higher in fracture strength, and one order of magnitude higher in electrical conductivity than the spin-coated nanofilm. Compared to wrinkled spin-coated nanofilms with orthogonal cracks, the crack-free, buckle-delaminated free-standing nanosheet shows not only stable electrical properties with high stretchability but also a large enhancement in both wetting anisotropy and parallel contact angle due to its higher-aspect-ratio features. Lastly, measuring the nanofilm's fracture strength and interfacial toughness from the metrology of cracking and buckle-delaminated micropatterns is demonstrated. It is shown that such metrology-based approaches can be applied to various nanofilm–substrate systems for thin film and interfacial mechanical properties measurement.

Organic conjugated polymers are known as conducting polymers with tunable electronic and mechanical properties through chemical modeling and synthesis,[1] which have found broad applications in organic integrated circuits, devices, and solar cells.[2] The semiconductive polymers are often low-cost, light-weight, and flexible. These outstanding properties make it a promising candidate for organic conjugated polymer–based stretchable and multifunctional electronics and devices,[3] where both robust mechanical properties and multifunctionality are highly desired.

The strategy of prestraining soft elastomeric substrates with spin-coated organic conjugated polymers has been used to generate wrinkling-based stretchable organic electronics.[4] However, these spin-coated organic polymer films often suffer from poor mechanical or electronic properties, as well as limited stretchability,[5] arising from the random distribution of polymer molecular chains during the spin-coating process.[6] These drawbacks largely hinder their applications in organic polymer-based multifunctional and stretchable electronics. Thus, new approaches are highly desired to enhance the mechanical performances of organic conjugated polymer films, as well as to augment their multifunctionality.

To this end, we propose a new fabrication approach to generate large-area, free-standing 2D organic conjugated polymeric P_3BT/C_{60} nanosheets. After transferring the free-standing nanosheet to a prestrained elastomeric substrate, we find a distinct surface instability in the form of periodic buckling-driven delamination, which is in contrast to the wrinkling pattern in its counterpart spin-coated nanofilms without debonding. We explore the mechanical, electrical, and wetting properties of both buckle-delaminated free-standing nanosheets and wrinkled spin-coated nanofilms. We find that compared to spin-coated nanofilms, the buckle-delaminated nanosheets demonstrate superior multifunctional performances, including high stretchability and high fracture strength, stable and high electrical conductance under an applied large strain, and larger degree of wetting anisotropy. Lastly, we show that the metrology of crack fragments and delaminated buckles provides an alternative way to measure thin film fracture strength and interfacial toughness, which can be generally applied to various nanofilm–substrate systems.

Figure 1 illustrates two different ways to fabricate buckled and stretchable P_3BT/C_{60} crystalline 2D nanofilms through the same prestrained substrate approach. One is in the form of coherent wrinkling of spin-cast thin films on the polydimethylsiloxane (PDMS) substrate without debonding (top row of Figure 1). The other is in the form of buckling-driven delamination of free-standing thin sheets due to their weak interfacial adhesion (bottom row of Figure 1).

Dr. Q. Zhang, Dr. Z. Zhang, Prof. J. Yin
Applied Mechanics of Materials Laboratory
Department of Mechanical Engineering
Temple University
1947 North 12th Street, Philadelphia, PA 19122, USA
E-mail: jieyin@temple.edu

The ORCID identification number(s) for the author(s) of this article can be found under https://doi.org/10.1002/admi.201900561.

DOI: 10.1002/admi.201900561

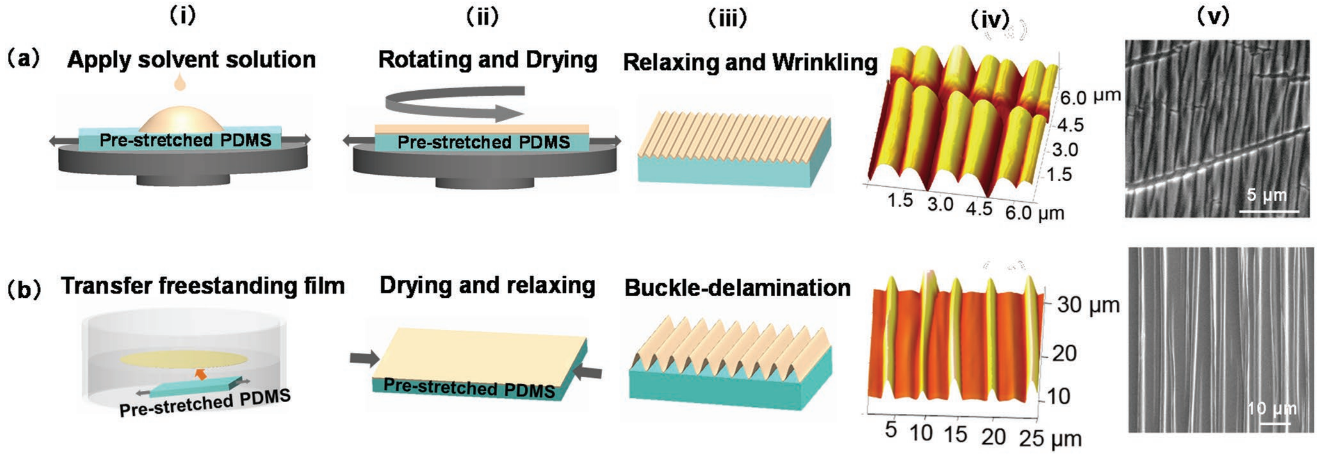

Figure 1. Two different fabrication methods of the same P_3BT/C_{60} nanofilm through spin-coating and transfer-printing generate distinct surface instabilities. a) i–iii) Schematics of generating wrinkled P_3BT/C_{60} nanofilms through spin-coating on prestretched PDMS substrates. Release of the prestrain (80%) leads to wrinkling micropatterns accompanied by cracks as shown in both the iv) AFM image and v) SEM image in the film with thickness of 60 nm. b) i–iii) Schematics of generating buckling-driven delaminated P_3BT/C_{60} nanosheets through transfer-printing of free-standing nanosheets to prestretched PDMS substrates. Release of the prestrain (80%) leads to crack-free, periodic buckle-delaminated micropatterns over large area as shown in both the iv) AFM image and v) SEM image in the sheet with thickness of 60 nm.

Figure 1a-i–iii schematically illustrates the spin-coating process to generate periodic wrinkles on the organic crystalline nanofilm. The P_3BT/C_{60} solutions were prepared with 1:5, 1,2-dichlorobenzene/toluene solvents, which can effectively balance the spreading and crystallization process of solutions (see the Experimental Section for more details).[6b] After depositing the solvent solution on a prestretched PDMS substrate, the substrate is spun rapidly to a desired rotating rate. After drying via solvent evaporation, a thin layer of nanoscale-thickness film will be generated on the substrate. The thickness of the fabricated spin-coated P_3BT/C_{60} crystalline film can be tuned in a range of 30–150 nm by controlling the rotating speed from 3000 rpm to 100 rpm. As a demonstration, we deposit a 2D P_3BT/C_{60} crystalline film with thickness $t = 60$ nm on a prestretched PDMS substrate with a prestrain of $\varepsilon_{\mathrm{pre}} = 80\%$. After releasing the prestrain in the substrate, a periodic wrinkling pattern is generated in the compressed spin-cast film along the stretching direction, as shown in both the atomic force microscopy (AFM) image and the scanning electron microscopy (SEM) image (Figure 1a-iv,v) of the periodic wrinkles (Figure S1, Supporting Information). Cracks with orthogonal orientation to the wrinkles are also observed in the spin-cast film due to the Poisson's effect–induced tensioning along the transverse direction (Figure S1c, Supporting Information).

Figure 1b-i–iii shows the process of generating buckling-driven delaminated patterns in the free-standing P_3BT/C_{60} nanosheet. A new water–air interfacial growth method is used to produce large-area, free-standing P_3BT/C_{60} nanosheets through self-assembly. The identical P_3BT/C_{60} solution as above is dropped on the deionized (DI) water, which spontaneously spreads over the aqueous surface. After slow evaporation of the solvent, free-standing P_3BT/C_{60} nanosheets, which are smooth, continuous, and compact, uniformly grow in the lateral direction. The thickness of P_3BT/C_{60} nanosheets mainly depends on the concentration of the spreading solution (see the Experimental Section for details). Figure S2a,b (Supporting Information) shows the transferred free-standing P_3BT/C_{60} nanosheets over a large area of 10 cm^2. Then a prestretched PDMS substrate is used to directly pick up the free-standing nanosheet formed on the water surface. We transfer the generated free-standing P_3BT/C_{60} nanosheet ($t = 60$ nm) to a prestretched PDMS substrate with $\varepsilon_{\mathrm{pre}} = 80\%$. After strain release, it forms a different periodic buckling-driven delaminated pattern due to its weak interfacial adhesion strength, which is shown in both the AFM image (Figure 1b-iv) and the SEM image (Figure 1b-v). Unlike the densely packed wrinkles on the spin-coated film (Figure 1a-iv), periodic localized delaminated blisters are observed across the free-standing nanosheet (Figure 1b-iv). The aspect ratio defined as the ratio of the wave amplitude to its wavelength in the delaminated blisters R_{d} ($R_{\mathrm{d}} \approx 0.56$) is about 1.5 times higher than that in the wrinkles R_{w} ($R_{\mathrm{w}} \approx 0.37$). In sharp contrast to the transversely cracked spin-coated film, there are no cracks observed on the free-standing nanosheet (Figure 1b-v) after the release of the same prestrain of 80% (Figure S2e,f, Supporting Information). The absence of cracks in the free-standing nanosheet implies its higher fracture strength than the spin-coated nanofilm.

With both exhibited improved fracture strength and high-aspect-ratio features in the freestanding nanosheet, next, we exploit its benefits for enhancing potential multifunctionality of organic P_3BT/C_{60} nanosheets in both electrical and wetting properties.

To evaluate how the electrical properties of both spin-coated and free-standing conductive organic films change with strain, we measure their normalized electrical resistance changes $\Delta R/R_{\mathrm{o}}$ as a function of the released strain in the PDMS substrate with the same $\varepsilon_{\mathrm{pre}} = 80\%$ (**Figure 2**, inset shows the schematic of the experimental setup), where R_{o} is the original electrical resistance of the unbuckled planar conductive coating. The thickness of both spin-coated film and free-standing sheet is set to be the same ($t = 120$ nm). Before prestrain release, we find that at the room temperature (23 °C), the electrical conductivity

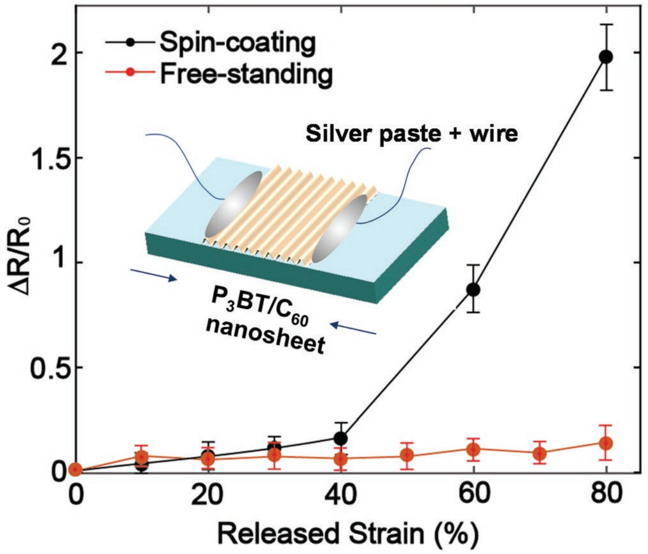

Figure 2. Electrical resistance change of both wrinkled and buckle-delaminated P_3BT/C_{60} nanofilms on PDMS substrates as a function of the released strain. The inset shows the schematic of experimental set-up for measuring the resistance.

of the free-standing planar P_3BT/C_{60} nanosheet is around 2.5×10^{-3} S m^{-1}, which is almost one order of magnitude higher than that of the spin-coated film. The lower conductivity in the spin-coated film is mainly attributed to the randomly distributed polymer chains and C_{60} molecules, which significantly decreases the charge transfer interaction between the polymer and the C_{60} molecules. In the transferred free-standing film, the fullerene molecules are mainly dispersed along the [100] direction between the adjacent polythiophene domains (closer to the S atoms[6b]). The charge transfer is occurring between the n orbitals of the S atoms in P_3BT and the π^*-orbitals of the C atoms in C_{60}. While in the spin-coated film, most of the C_{60} molecules are randomly distributed throughout the film with weak interactions with P_3BT molecules. Figure 2 shows that during the initial prestrain release, the electrical resistance of the wrinkled spin-coated P_3BT/C_{60} film increases slightly with $\Delta R/R_o < 0.2$. However, when the released strain is beyond 40%, its resistance increases dramatically to be one order higher due to the occurrence of transverse cracking in the wrinkled film. In contrast, over the whole process of full strain release, the electrical resistance of the free-standing buckle-delaminated nanosheet remains almost unchanged and stable with $\Delta R/R_o < 0.1$. The stable resistance is mainly attributed to its higher fracture strength, where no cracking fragmentation is observed over the whole sample (Figure S2e,f, Supporting Information).

Next, we exploit how the increased aspect ratio of blisters in the buckle-delaminated P_3BT/C_{60} sheet impacts its wetting behavior. To compare with its counterpart wrinkled P_3BT/C_{60} film, both film thickness (t = 80 nm) and the substrate prestrain ($\varepsilon_{\text{pre}} = 100\%$) are set to be the same.

The top row of **Figure 3**a shows the isotropic and hydrophilic wetting behavior of a 5 µL droplet on the planar spin-coated and free-standing films before releasing the prestrain, where the static contact angle of the spin-coated film (80°) is slightly higher than that of the free-standing sheet (71°). After the prestrain release, both buckled films show an anisotropic and hydrophobic wetting behavior due to their highly anisotropic and high-aspect-ratio grooved surface features.[7] We observe that the water droplets elongate along the grooves of the wrinkles or blisters. The static contact angles of the anisotropic water droplets are measured in two directions: parallel ($\theta_{//}$) and perpendicular ($\theta_{\perp}$) to the wrinkle/blister orientation, which are shown in the inset of Figure 3b. For both coatings, the contact angles in both directions increase dramatically to be over 120° after wrinkling or buckle-delamination. Specially, for the free-standing sheet, $\theta_{//}$ becomes doubled after buckling ($\theta_{//} = 143°$). The increase in $\theta_{//}$ ($\Delta\theta_{//} = 72°$) is over 20° higher than that of the wrinkled film ($\Delta\theta_{//} = 50°$), making it become even more hydrophobic than its counterpart wrinkled surface. This agrees with previous report on the enhanced hydrophobic effect through increasing the aspect ratio of micro-wrinkles generated through UVO treatment on prestrained PDMS substrates.[8]

The wetting anisotropy is defined as the contact angle difference between the two orthogonal directions, i.e., $\Delta\theta = \theta_{//} - \theta_{\perp}$. The buckle-delaminated free-standing sheet exhibits a higher degree of wetting anisotropy with $\Delta\theta = 23°$, which is over twice larger than the wrinkled surface ($\Delta\theta = 11°$). It should be noted that both wrinkles and cracks contribute to the wetting behavior of the wrinkled film since the transverse cracks expose the underlying hydrophobic PDMS substrate,[7] whereas the wetting behavior of the crack-free buckle-delaminated sheet is mainly determined by its buckled surface features. Thus, compared to the wrinkled film, the large enhancement in both degree of wetting anisotropy and parallel contact angle in the buckle-delaminated sheet is mainly attributed to its higher aspect ratio of the blisters, which is consistent with previous studies on the enhanced effect of high-aspect-ratio surface features on the wetting anisotropy.[7,8]

We notice that the transition from the buckled hydrophobic state to its original unbuckled hydrophilic state is reversible and switchable in both films through simply restretching/releasing the substrate prestrain. Figure 3b shows that upon restretching both buckled films, the large contact angles in both directions reduce gradually to be below 90° and the degree of wetting anisotropy $\Delta\theta$ is also becoming smaller. After restretching to 100%, which is the same magnitude as the prestrain, both wrinkles and blisters become flattened and the contact angle reaches its original value with $\Delta\theta$ being close to 0°. Specially, the contact angle of the free-standing sheet along the parallel direction shows the largest drop by over 70° due to its higher aspect ratio feature. The reversible wettability transition for both buckled films is further confirmed under cyclic loading/unloading by repeatedly restretching and releasing the substrate. Figure 3c shows that their contact angles along both parallel and perpendicular directions under both unbuckled and buckled states remain almost unchanged with the increasing cycles of the applied mechanical strain. It also demonstrates that the tunable wetting in the free-standing sheet can be manipulated in a much larger range than the spin-coated film under the same applied mechanical strain.

The mechanical properties and buckle-delaminated features of the organic semiconducting polymer sheet underpin its multifunctional electrical and wetting performances, including the stiffness, fracture strength, and adhesion strength. So far, we

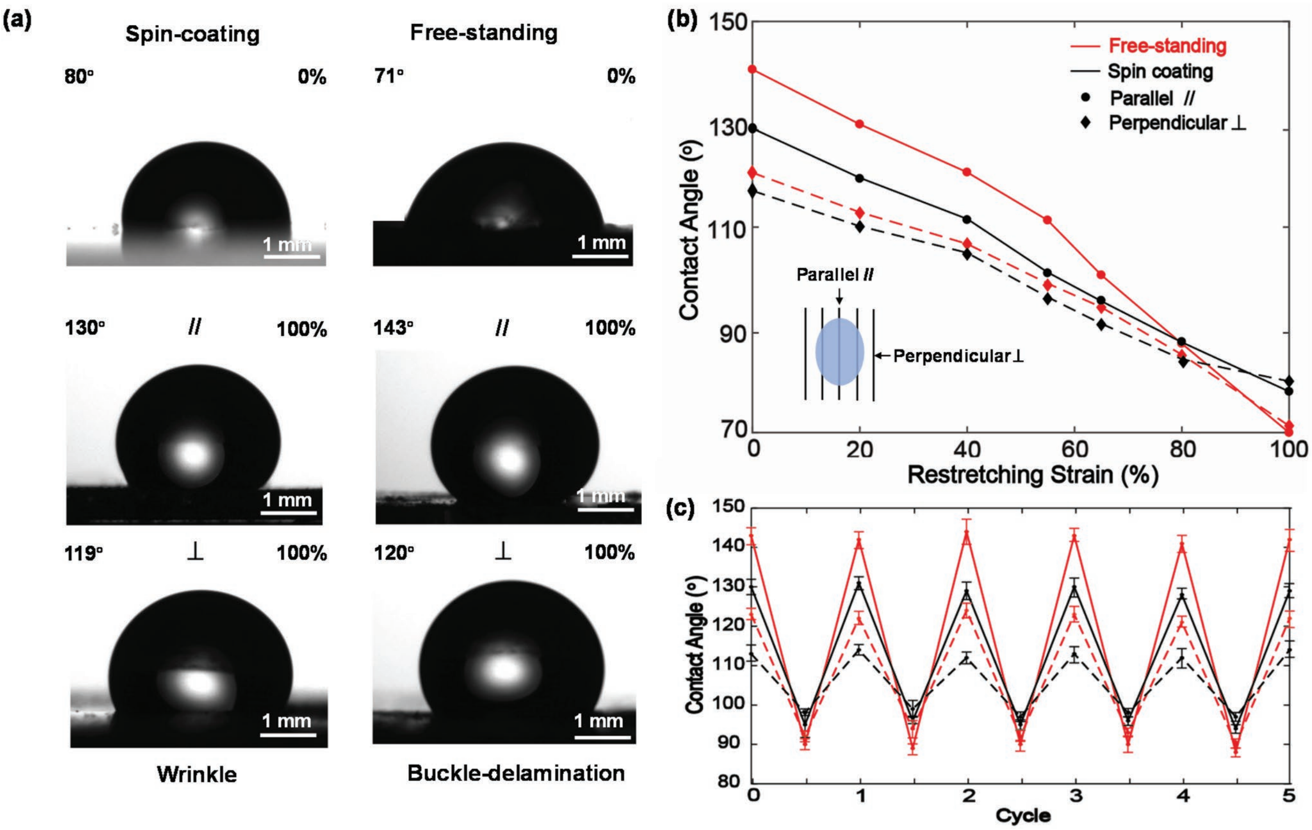

Figure 3. Comparison of wetting behavior between wrinkled spin-coated nanofilm and buckle-delaminated free-standing P_3BT/C_{60} nanosheet on PDMS substrates. a) Top row: side views of a droplet on flat spin-coated and free-standing nanofilms before release of the substrate prestrain. Middle and bottom row: side views of a droplet oriented to the parallel (middle) and perpendicular (bottom) direction of the wrinkles. b) Contact angle change in both perpendicular and parallel directions on wrinkled spin-coated and free-standing buckle-delaminated surfaces as a function of the restretching strain. The inset shows the schematic of measuring both parallel and perpendicular contact angles on a wrinkled surface. c) Reversible switching in the contact angles for both wrinkled and buckle-delaminated films in both directions after five cycles of substrate prestrain releasing and restretching.

have shown that the P_3BT/C_{60} film fabricated through the proposed water–air interfacial growth method exhibits stable electrical resistance due to its higher fracture strength and larger range of tunable wettability through buckle-delamination. Next, we will rely on the developed theoretical models on wrinkling and buckle-delamination of thin films to quantify the mechanical properties of both films fabricated from different methods.

It shows that two different fabrication methods of the same organic polymeric thin films can result in distinct elastic modulus. The measurement of elastic modulus of the spin-coated P_3BT/C_{60} film can be obtained from the metrology of its wrinkled morphologies.[9] By fitting the measured wrinkling wavelength with the theoretical wrinkling model considering the finite deformation in the film under large substrate prestrain, the elastic modulus of spin-coated P_3BT/C_{60} film is calculated as $E_f \sim 2.4 \pm 0.1$ GPa for films with thickness ranging from 30 to 100 nm (Figure S3a, see Supporting Information for details). The characterization of the elastic modulus of the free-standing P_3BT/C_{60} film through nanoindentation shows that its modulus is over five times higher than that of the spin-coated film with thickness ranging from 60 to 150 nm (Figure S3b, Supporting Information).

Similarly, from the measurement of the metrology of cracking fragments, the critical fracture strength of both P_3BT/C_{60} thin films can be calculated and estimated based on the simple theoretical cracking model of thin films on soft substrates.[10] Here, we assume that the maximum tensile stress occurs at the midpoint of a fragment. By measuring the average width of cracked strips d (**Figure 4**a), the critical fracture strength σ_c of thin films can be estimated as[10]

$$\sigma_c = \frac{E_s\left(\nu_s\varepsilon_{pre} - \varepsilon_c\right)d}{2t} \approx \frac{E_s\nu_s\varepsilon_{pre}d}{2t} \tag{1}$$

where ε_c is the onset fracture strain of the thin film with $\varepsilon_c \ll \varepsilon_{pre}$ given $\varepsilon_{pre} \geq 80\%$. E_s and ν_s are the respective Young's modulus and Poisson's ratio of the soft substrate. t is the film thickness.

To explore the fracture strength of the free-standing P_3BT/C_{60} nanosheet, we increase the substrate prestrain from 80% to 120%, which approaches to the fracture strain of the PDMS substrate (about 150%). Similar parallel cracking fragmentations are observed in the wrinkled spin-coated film (Figure 4a). Surprisingly, there is still no transverse cracking observed in the buckle-delaminated sheet (Figure 4b), implying that its maximum tensile stress in the free-standing nanosheet is still below its critical fracture strength. To approach its fracture strength, we further significantly increase the substrate

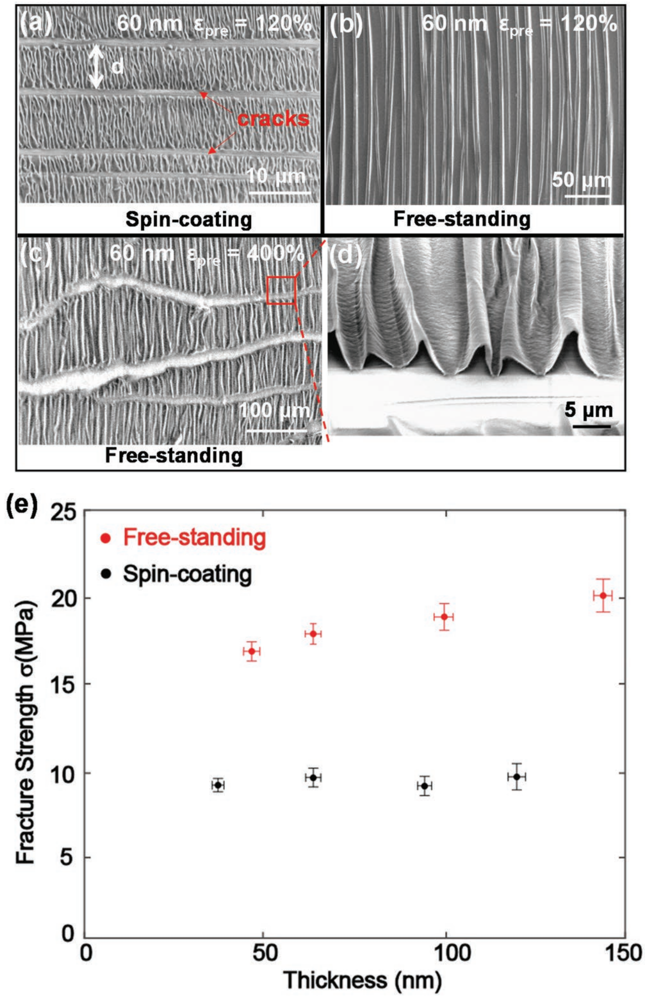

Figure 4. Fracture strength measurements for spin-coating and free-standing P$_3$BT/C$_{60}$ nanofilm. a,b) SEM images of a cracked, wrinkled spin-coating a) and crack-free, buckle-delaminated free-standing nanosheet b) with the same thickness of 60 nm on PDMS substrates with $\varepsilon_{pre} = 120\%$. c,d) SEM images of cracked free-standing nanosheet with thickness of 60 nm on Ecoflex substrates with ε_{pre} = 400% with magnified view of the SEM image of buckle-delaminated sheet at the cracked region in (d). e) Fracture strength of both spin-coating and free-standing P$_3$BT/C$_{60}$ films with different thickness.

prestrain to 400% by replacing the PDMS substrate with a more stretchable elastomer (Ecoflex 00-05; Smooth-on, Inc.). Upon the prestrain release, transverse cracking fragments are observed as shown in Figure 4c. A high-resolution SEM image in Figure 4d shows the detailed cross-section profile of the exposed periodic delaminated buckles at the cracked region.

Based on the measured metrology of the cracked fragments, we plot the calculated fracture strength from Equation (1) for both spin-coated and free-standing P$_3$BT/C$_{60}$ nanofilms with different coating thickness in Figure 2e, where the measured Young's modulus E_s of Ecoflex and PDMS is 15 kPa and 2 MPa, respectively, and ν_s = 0.49 is the same. It shows that the fracture strength for both films remains almost unchanged for film thickness varying from 40 to 150 nm, where σ_c in the free-standing sheet (18.7 ± 1.0 MPa) is almost twice higher than the spin-coated film (9.9 ± 0.5 MPa).

The enhanced mechanical properties of the free-standing P$_3$BT/C$_{60}$ sheet can be attributed to its distinct chemical structures from the spin-coated film. Unlike spin-coated P$_3$BT/C$_{60}$ film with randomly distributed polymer chains and C$_{60}$ molecules, the self-assembly free-standing P3BT/C60 sheet possesses the orthorhombic symmetry, similar to the pure ordered P3BT film.[11] It indicates that the main structure is composed of crystalline polythiophene chains, which are parallel with the substrate.[12] The schematic illustrations of the orientation of the polymer chains in spin-coated and transfer-printed films are shown in Figure S4 (Supporting Information). The C$_{60}$ molecules are mainly dispersed along the [100] direction between the adjacent polythiophene domains. Therefore, it enables remarkable π–π interactions between the polymer chains in the sheet, which leads to higher mechanical strength in the free-standing P$_3$BT/C$_{60}$ sheet.

In addition to the mechanical properties of the P$_3$BT/C$_{60}$ films, the adhesion strength between the organic polymeric film and the soft substrate plays an important role in determining the surface instability modes and the structural integrity. Similarly, from the metrology of the periodic buckle-delaminated micropatterns, we can measure the interfacial toughness between the free-standing P$_3$BT/C$_{60}$ sheet and the PDMS substrate. Typically, the interfacial toughness is defined as the adhesion energy required to separate thin films from the substrate. Traditional measurement methods such as Kendall's peel testing,[13] scratch testing,[14] and pressured blister testing[15] are typically used to measure the interfacial toughness between the thin film and the underlying stiff substrate. However, it remains challenging for such approaches to be directly applied to measure the interfacial toughness of thin films on soft elastomeric substrate. Recently, we proposed an alternative method to measure the interfacial toughness from the metrology of buckle delamination.[5] For spontaneous periodic buckling-driven delamination of thin films on prestrained soft substrates, the width λ of the periodic delaminated blisters can be predicted as[5]

$$\lambda = \pi t \sqrt{\frac{\bar{E}_f t}{\Gamma}} \sqrt{\frac{\varepsilon_{pre}}{1+\varepsilon_{pre}}} \tag{2}$$

where $\bar{E}_f = E_f/(1-\nu_f^2)$ is the plane strain modulus of the film with E_f and ν_f being Young's modulus and Poisson's ratio, respectively. Γ is the interfacial toughness. From Equation (2), based on the profile of periodic buckle-delaminated blisters, the estimation of the interfacial toughness Γ can be expressed as

$$\Gamma = \frac{\pi^2 \bar{E}_f t^3}{\lambda^2}\left(\frac{\varepsilon_{pre}}{1+\varepsilon_{pre}}\right) \tag{3}$$

To calculate the interfacial toughness between the free-standing P$_3$BT/C$_{60}$ sheet and the PDMS substrate, we can experimentally measure the width λ of the periodic delaminated blisters as a function of thin sheet thickness t under the same ε_{pre} = 80% as shown in **Figure 5**a. The inset of Figure 5a shows an example of the cross-sectional profile of the delaminated free-standing sheet with $t = 120$ nm measured by AFM. With measured data of λ and t, the interfacial toughness can be calculated from Equation (3) and is plotted as black scattered points (with error bars) in Figure 5a. We observe that these calculated data float in a reasonable small range and the interfacial toughness shows an average value of 2.44 ± 0.5 J m^{-2}. We note that such an approach is not limited to measuring the mechanical and interfacial properties of polymeric films studied here, but can be readily applied to different inorganic nanofilms on soft substrates. As an example, we estimate both interfacial toughness Γ and fracture strength σ_c of Au and Cu nanofilms by depositing thin films with different thickness on prestrained soft elastomeric substrates (see Supporting Information for more details). The results of the analysis are presented in Figure S5 (Supporting Information), which shows a good agreement with the reported values in previous studies measured by different methods.[10a,15b,16]

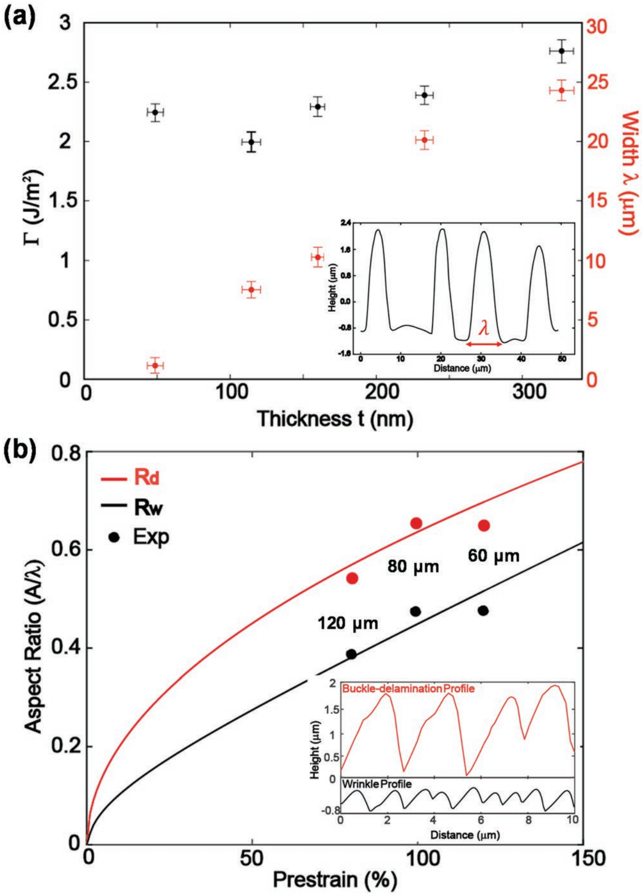

Figure 5. a) Measured interfacial toughness Γ between the free-standing P_3BT/C_{60} nanosheet and the PDMS substrate and the width λ of periodic delaminated blisters as a function of nanosheet thickness t. Inset shows the AFM cross-sectional view of the height profile of blisters with $t = 120$ nm and $\varepsilon_{pre} = 80\%$. b) Comparison of the aspect ratio of wrinkles and delaminated blisters in both nanofilms as a function of the prestrain ε_{pre}. Inset shows the AFM measured step height profile of delaminated blisters and wrinkles in the spin-coated and free-standing nanofilms on PDMS substrates with $t = 60$ nm and $\varepsilon_{pre} = 120\%$.

Compared to the strong adhesion strength in the wrinkled spin-coated P_3BT/C_{60} film, the benefit of weak interfacial toughness is to achieve higher-aspect-ratio surface features through buckle-delamination, which has shown to enhance both the large hydrophobicity and tunable wetting of the buckled surfaces as discussed above. Theoretically, for both wrinkling and buckle-delamination of thin films on a soft substrate, the aspect ratio of wrinkles R_w and blisters R_d can be given by[5,17]

$$R_w \approx \frac{1}{\pi}\sqrt{\varepsilon_{pre}\left(1+\varepsilon_{pre}\right)} \tag{4}$$

$$R_d = \frac{2}{\pi}\sqrt{\varepsilon_{pre}} \tag{5}$$

given the large prestrain over 80% and large film–substrate modulus ratio $\overline{E}_f/\overline{E}_s$ of over 10^3 for the studied case of P_3BT/C_{60} film on PDMS substrates. Equations (4) and (5) show that the aspect ratios of both wrinkles and delaminated buckles are independent of material properties and the geometry of the film–substrate system and are only governed by the substrate prestrain ε_{pre}.

Next, we compare the aspect ratio of both generated wrinkles and delaminated buckles as a function of ε_{pre} in Figure 5b. It shows that both R_w and R_d increase nonlinearly and monotonically with ε_{pre}. More importantly, the aspect ratio of delaminated buckles is much higher than that of the wrinkles under the same ε_{pre}, especially when ε_{pre} is relatively larger. Experimental measurements on the aspect ratios of both wrinkles (spin-coated film) and blisters (free-standing sheet) with different thickness are consistent with the theoretical prediction (Figure 5b). As an example, the inset of Figure 5b shows the comparison of the cross-sectional profiles between wrinkled spin-coated and buckle-delaminated free-standing P_3BT/C_{60} films with the same $t = 80$ nm and $\varepsilon_{pre} = 100\%$. It shows that compared to the small-size wrinkles (highlighted in black color) with shallow features ($\lambda \approx 1.2$ μm and $A \approx 560$ nm), the large-size blisters (highlighted in red color) are sharper with much higher amplitude ($\lambda \approx 3.1$ μm and $A \approx 2$ μm). The blisters show a higher aspect ratio ($R_d \approx 0.65$) than the wrinkles ($R_w \approx 0.47$), leading to the observed higher hydrophobic contact angle and larger degree of wetting anisotropy in Figure 3.

In conclusion, we developed a new fabrication strategy to generate stretchable organic semiconducting polymeric systems by forming buckle-delamination of free-standing organic conjugated polymeric (P_3BT/C_{60}) nanosheets on a soft elastomeric substrate. Compared to wrinkling of spin-coated P_3BT/C_{60} nanofilms, the buckle-delaminated free-standing nanosheet shows largely enhanced mechanical properties and higher-aspect-ratio surface features, which enable a potentially higher stretchability with more stable electrical performance and a wider range of tunable wettability. The results of this research could find potential applications in the design of highly stretchable organic conducting devices, micropatterned high-aspect-ratio surfaces with tunable extreme surface properties in wetting, adhesion, and friction, as well as measuring the mechanical and interfacial properties of thin films on soft substrates systems through the buckled and cracked metrology.

Experimental Section

Fabrication of Elastomer Substrates: PDMS substrates with the thickness of 3 mm were prepared by mixing PDMS Sylgard 184 (Dow Corning Corporation), prepolymer, and cross-linker at 10:1 weight ratio. The PDMS solution was cured at 60 °C for 4 h in a Petri dish and then cut and cleaned with isopropyl alcohol. The elastomer substrate (Ecoflex 00-05; Smooth-on, Inc.) with a thickness of 3 mm and 15 kPa modulus was used for achieving higher stretchability and fracture strength measurement.

Fabrication of P_3BT/C_{60} Nanofilms on Elastomer Substrates through Spin-Coating Deposition: Orthodichlorobenzene/toluene mixed solvent was prepared to dissolve the organic compounds. The mixed solvent (0.4 mL) with 0.4–20 g L^{-1} solute concentration was dropped on the prestrained and plasma-treated PDMS surfaces, which was fixed on a KW-4A spin coater. The spin-coating films with thickness from ≈30 to 150 nm were generated by varying the spinning rotation speed from 3000 to 100 rpm. Two ways were employed to minimize the swelling phenomenon of PDMS induced by toluene: one was to treat the PDMS with an air-condition plasma to generate a layer of SiO_2 at the surface, the other was to reduce the toluene contacting time with the PDMS through high rotation speed during the spin-coating process.

Fabrication of P_3BT/C_{60} Nanosheet on Elastomer Substrates through Free-Standing Transfer: To synthesize high-quality free-standing P_3BT/C_{60} polymer nanosheet, a novel interfacial self-assembling method was applied through evaporating the mixed solvent, the same as the one prepared in the spin-coating process at 181 °C boiling temperature. The Petri dishes with a diameter of 6 cm were cleaned by toluene/acetone and plasma treated for 10 min and then filled with DI water. 0.4 mL mixed solvent with 0.4–20 g L^{-1} solute concentration was dropped on the DI water surface. After spreading and evaporating of the solvent, free-standing P_3BT/C_{60} polymer nanosheets are formed gradually in the lateral direction. Finally, the free-standing film can be directly picked up by the prestretched elastomeric substrate.

Characterization of Surface Topography: Dimension icon AFM at tapping mode was used to quantify wrinkle/buckle topographies via a Cr/Pt-coated nano silicon probe (radius < 25 nm, resonant frequency ≈13 kHz, NCHV-A, BurkerNano). FEI Quanta 450FEG with low vacuum mode was used to take SEM images at a 10 kV acceleration voltage. For each sample, at least five measurements were taken to confirm the repeatability.

Contact Angle Measurement: Rame-hart Model 260 Standard Contact Angle Goniometer was used to measure the static contact angles at room environment temperature 22 °C and humidity of 23%. In all contact angle measurements, a 5 µL liquid droplet was gently placed on different surfaces and then measured by software.

Electrical Resistance Test: After transferring thin films on prestretched substrates, silver paste and fine wire at both ends to measure the electrical resistance were used. Then, the samples were released step by step to measure their electrical resistance changes as a function of the applied compression strain.

Statistical Methods: For each experiment, statistical analyses were used to show the experimental uncertainty of the measurement. The error bars were corresponded to standard deviations of the means for at least five group measurements.

Supporting Information

Supporting Information is available from the Wiley Online Library or from the author.

Acknowledgements

J.Y. acknowledges the funding support from the National Science Foundation (NSF) (CMMI-1727792) and (CMMI-1745921).

Conflict of Interest

The authors declare no conflict of interest.

Keywords

buckling-driven delamination, multifunctionality, organic conducting nanofilms, organic stretchable devices, wrinkling

Received: March 28, 2019
Revised: May 16, 2019

---

[1] a) A. Facchetti, *Chem. Mater.* **2010**, *23*, 733; b) Y.-J. Cheng, S.-H. Yang, C.-S. Hsu, *Chem. Rev.* **2009**, *109*, 5868; c) J. Roncali, *Chem. Rev.* **1992**, *92*, 711.
[2] a) A. Darwish, A. E. Hassanien, *Sensors* **2011**, *11*, 5561; b) M. Toivola, M. Ferenets, P. Lund, A. Harlin, *Thin Solid Films* **2009**, *517*, 2799; c) C. Pang, C. Lee, K. Y. Suh, *J. Appl. Polym. Sci.* **2013**, *130*, 1429; d) S. Savagatrup, A. S. Makaram, D. J. Burke, D. J. Lipomi, *Adv. Funct. Mater.* **2014**, *24*, 1169.
[3] a) S. E. Root, S. Savagatrup, A. D. Printz, D. Rodriquez, D. J. Lipomi, *Chem. Rev.* **2017**, *117*, 6467; b) T. Sekitani, H. Nakajima, H. Maeda, T. Fukushima, T. Aida, K. Hata, T. Someya, *Nat. Mater.* **2009**, *8*, 494.
[4] Y. Lee, H. Zhou, T.-W. Lee, *J. Mater. Chem. C* **2018**, *6*, 3538.
[5] Q. Zhang, J. Yin, *J. Mech. Phys. Solids* **2018**, *118*, 40.
[6] a) L. Ruan, D. Zhang, J. Tong, J. Kang, Y. Chang, L. Zhou, G. Qin, X. Zhang, *Ferroelectrics and Their Applications*, IntechOpen, London, UK **2018**; b) Z. Zhang, H. Li, R. Miller, H. Malissa, S. Jamali, C. Boehme, J. C. Grossman, S. Ren, *Nano Lett.* **2018**, *18*, 4346.
[7] G. Lin, Q. Zhang, C. Lv, Y. Tang, J. Yin, *Soft Matter* **2018**, *14*, 1517.
[8] J. Y. Chung, J. P. Youngblood, C. M. Stafford, *Soft Matter* **2007**, *3*, 1163.
[9] a) G. Lin, P. Chandrasekaran, C. Lv, Q. Zhang, Y. Tang, L. Han, J. Yin, *ACS Appl. Mater. Interfaces* **2017**, *9*, 26510; b) C. J. Brennan, J. Nguyen, E. T. Yu, N. Lu, *Adv. Mater. Interfaces* **2015**, *2*, 1500176; c) X. Chen, J. Yin, *Soft Matter* **2010**, *6*, 5667; d) Y. Sun, W. M. Choi, H. Jiang, Y. Y. Huang, J. A. Rogers, *Nature Nanotechnol.* **2006**, *1*, 201.
[10] a) Q. Zhang, Y. Tang, M. Hajfathalian, C. Chen, K. T. Turner, D. A. Dikin, G. Lin, J. Yin, *ACS Appl. Mater. Interfaces* **2017**, *9*, 44938; b) S. Bazhenov, A. Volynskii, V. Alexandrov, N. Bakeev, *J. Polym. Sci. B* **2002**, *40*, 10.
[11] A. Buono, N. H. Son, G. Raos, L. Gila, A. Cominetti, M. Catellani, S. V. Meille, *Macromolecules* **2010**, *43*, 6772.
[12] S. Chen, X. Li, K. Yao, F. E. H. Tay, A. Kumar, K. Zeng, *Polymer* **2012**, *53*, 1404.
[13] K. Kendall, *J. Phys. D: Appl. Phys.* **1975**, *8*, 1449.
[14] a) S. Venkataraman, D. L. Kohlstedt, W. W. Gerberich, *J. Mater. Res.* **2011**, *7*, 1126; b) S. K. Venkataraman, D. L. Kohlstedt, W. W. Gerberich, *J. Mater. Res.* **2011**, *8*, 685.
[15] a) Z. Cao, P. Wang, W. Gao, L. Tao, J. W. Suk, R. S. Ruoff, D. Akinwande, R. Huang, K. M. Liechti, *Carbon* **2014**, *69*, 390; b) A. Volinsky, N. Moody, W. Gerberich, *Acta Mater.* **2002**, *50*, 441.
[16] a) X. Li, B. Bhushan, K. Takashima, C.-W. Baek, Y.-K. Kim, *Ultramicroscopy* **2003**, *97*, 481; b) P. A. Gruber, J. Böhm, F. Onuseit, A. Wanner, R. Spolenak, E. Arzt, *Acta Mater.* **2008**, *56*, 2318.
[17] H. Jiang, D.-Y. Khang, J. Song, Y. Sun, Y. Huang, J. A. Rogers, *Proc. Natl. Acad. Sci. U. S. A.* **2007**, *104*, 15607.